PFC/JA-85-44

JANUS, A BI-DIRECTIONAL, MULTI-FUNCTIONAL PLASMA DIAGNOSTIC

A. S. Wan, T. F. Yang, B. Lipschultz, B. LaBombard

December 1985

This work was supported by the U.S. Department of Energy Contract No. DE-AC02-78ET51013. Reproduction, translation, publication, use and disposal, in whole or in part by or for the United States government is permitted.

Submitted for publication in: Review of Scientific Instruments

ABSTRACT

Janus, a Bi-Directional, Multi-Functional Plasma Diagnostic

A. S. WAN, T. F. YANG, B. LIPSCHULTZ, B. LaBOMBARD

Plasma Fusion Center, M.I.T.

Janus is a multiple function edge probe used to diagnose the Alcator C limiter shadow plasma whose components include two sets of identical diagnostics; each set facing a different direction. Included within each set of diagnostics are a retarding-field energy analyzer (RFEA), Langmuir probe, and calorimeter. Janus is constructed to make measurements both parallel and antiparallel to a magnetic field. It can withstand high heat fluxes and can be scanned perpendicular to the magnetic field in the limiter shadow. The RFEA can alternatively sample both the ion and electron parallel energy distribution functions during a tokamak discharge. From the Langmuir probe, one can infer electon temperature, density, and the plasma floating potential. The calorimeter independently detects the total parallel heat flux incident on an electrically floating plate. Together these three diagnostics enable detailed, localized edge plasma studies on Alcator C. This paper presents the design considerations for each of the diagnostics along with a brief summary of the analysis techniques. Some experimental results obtained using Janus will also be presented.

Introduction

The edge of a tokamak plasma plays an important role in the performance of the bulk plasma. H-Mode confinement[1,2,3] and Marfes[4,5] are two examples of edge phenomena that can affect the bulk plasma behavior of tokamaks. To gain further understanding of processes at the plasma edge that can drive such phenomena it is important to diagnose this region in more detail.

The particle and heat fluxes flowing along a field line are also of particular interest. Those measurements can be used to predict material damage due to plasma-surface interaction processes such as evaporation and physical sputtering from surfaces within the vacuum vessel[6,7]. The evaluation of surface material integrity is important from the point of view of plasma purity and vessel lifetime.

Manos and McCracken[8] and Cohen[9] have recently summarized edge diagnostic capabilities. Most of the previous edge plasma studies employed either an array of single purpose diagnostics or tried to piece together information from different diagnostics at different toroidal or poloidal locations. However, many tokamaks have observed strong poloidal[4,5,10,11] and toroidal[12,13,14] asymmetries of edge plasma parameters. Consequently, a proper correlation between various edge parameters requires a local, directional measurement. A number of "essential" edge parameters which need to be recorded in this localized manner are ion and electron energy distribution functions, densities, local potentials, heat fluxes, and their fluctuations. Ideally, one would like to measure all these "essential" edge plasma parameters at many spatial locations. However this task is formidable and difficult even at only one spatial position.

We have developed a multi-functional edge diagnostic set for use on Alcator C herein denoted by Janus which simultaneously measures the edge plasma parameters listed above at one spatial position. Janus is a bi-directional probe with two identical sets of diagnostics: one set facing the ion side and one facing the electron side (as defined by the plasma current, I_p) along the background toroidal magnetic field. Each set of diagnostics includes a retarding-field energy analyzer (RFEA), a Langmuir probe, and a calorimeter.

The first section of this paper briefly describes the Alcator C tokamak, the Janus experimental set-up, and some general Janus design considerations. Section 2, 3 and 4 present general design considerations and analysis techniques of the calorimeter, the RFEA and the Langmuir probe respectively. Section 2 also contains some typical results of the calorimeter. Section 5 shows a time history of the RFEA and Langmuir probe measurements for a single Alcator C discharge. The details of plasma physics implications due to the experimentally observed phenomena obtained by Janus are beyond the scope of this paper and are deferred to later publications. However, a number of important observations are pointed out in section 5. Finally, brief summary is presented in section 6.

1.1 Alcator C

Table 1 summarizes typical operating parameters of the Alcator C tokamak device. Major experiments carried out on Alcator C include RF heating and current drive[15,16], pellet injection[17,18], impurity injection and transport analysis[18,19]. The utilization of Bitter-type magnets enables Alcator C to operate at high field and high density. Such a design has allowed it to become the first fusion device to surpass the Lawson Criterion[17]. However this design also results in small port access geometry which becomes a difficult constraint in developing diagnostics.

1.2 Janus Set-Up and General Considerations

Figure 1 shows an unscaled artist's conception of the experimental set-up of Janus looking perpendicular to its "viewing" length along a field line. Typically Janus is inserted from the top of Alcator C, directly centered over the magnetic axis. It can be scanned in the minor radial direction (perpendicular to the magnetic field). The motion is limited by the vacuum wall at one extreme and the limiter radius defining the main plasma edge at the other extreme. The geometrical center of the diagnostic apertures are recessed about 0.5 cm from the leading edge of the probe.

Alcator C typically operates with two sets of full poloidal ring limiters. For the sake of easy labelling, we define the two sides of Janus in accordance with the plasma current direction. Therefore, as indicated by figure 1, the Janus electron side flux tube has a limiter connection length that is twice as long as the ion side.

The probe casing is large such that its natural perturbing length[20,21] is much longer than the corresponding limiter connection length. Therefore it is a "perturbing probe", behaving more or less like an independent limiter block.

Janus is constructed with a molybdenum casing and Al_2O_3 insulators to operate at high temperature. In addition, in order to allow for easy maintenance, the probe head is detachable. The head assembly and detachment scheme is sketched in figures 2 and 3. The connections between the wires originating from the probe head and the wires from the vacuum feedthrough are achieved using Be-Cu spring electrodes confined by carefully machined matching slot insulators.

Figure 2 shows a 3-D view of a set of diagnostics on a single side of Janus. The retarding-field energy analyzer is flanked by the Langmuir probe on the inside (smaller major radius) and the calorimeter on the outside. A U-shape spring is inserted between the two sets of diagnostics in order to secure all components in place. The entire Janus probe head is less than 1 inch perpendicular (poloidal) and $1\frac{7}{8}$ inches parallel (toroidal) to the view shown in figure 1.

The associated electronics are all grounded at one point on the Alcator C vacuum vessel with electrically isolated cable trays supporting the wires between the probe and the electronics. The signals are digitized at 10 kHz using a LeCroy 8212 CAMAC module. Optic fibers provide the link between the electrically isolated CAMAC module and the data acquisition system.

Design considerations, analysis techniques, and some typical experimental results of the calorimeter, RFEA, and Langmuir probe are now discussed in turn.

2. Calorimeter

2.1 Design Consideration

The calorimeter is designed to infer the parallel plasma heat flux, $q_{||}(t)$, incident onto an electrically floating plate. The design is divided into two separate sections: the thermocouple and the calorimeter plate.

For operation at high temperatures, three types of thermocouples were considered: chromel-alumel, tungsten-rhenium, and platinum-rhodium. Platinum-rhodium is easily reduced and can only operate in a vacuum for a very short period of time. Tungsten-rhenium is easily oxidized and is extremely brittle. In addition, both of these thermocouples have smaller change of induced emf per degree temperature rise as compared with the chromel-alumel thermocouple. Chromel-alumel is also very easy to machine, enabling us to use the flat ribbon-type thermocouples for our calorimeter which minimizes the thermal response time. Therefore, despite a lower operating temperature limit, chromel-alumel thermocouple was chosen over the other candidates.

The calorimeter plate must have fast thermal response properties while still being able to withstand high heat fluxes. As a first approximation, we can analytically estimate a thermal response time, $\tau_{response}$, using an infinite thin plate approximation[22] and obtain:

$$\tau_{response} = \frac{\rho_m \; C_p \; \delta^2}{2 \; k}, \tag{1}$$

where ρ_m is the material mass density, C_p the heat capacity, k the thermal conductivity, and δ the plate thickness. In actuality, our calorimeter design exposes only about 40% of the total plate area to the incident plasma. As a refinement of the above approximation we can replace δ with the ratio of the plate volume over the exposed area. However, to properly predict $\tau_{response}$, the implicit 3-D heat transport that results from this design should be examined in more detail. The effect of the thermocouple welded at the rear of the plate must also be considered in estimating the final response time. The exact determination of $\tau_{response}$ is not critical in that its value does not affect the accuracy of the data analyzed.

A 0.635 mm tungsten calorimeter plate was chosen instead of molybdenum, tantalum, or TZM due to its overall thermal properties and high melting point ($\sim 3600°K$). However, the utilization of a chromel-alumel thermocouple limits the operating temperature ($\sim 1640°K$). Plugging in the design parameters to equation 1, we obtain an estimated $\tau_{response}$ of 15-20 msec. Using a simple energy balance, the calorimeter can easily withstand over 1 kW/cm^2 during the entire Alcator C discharge (lasting $\sim$ 500 ms).

2.2 Analysis Technique

The analysis of the calorimeter output follows the treatment of Manos, et. al.[23] A change in temperature of the calorimeter plate is principally caused by three processes: the plasma heat flux, radiation loss from the hotter plate to a cooler vacuum vessel surface, and conduction loss from the hot plate to a cooler probe box. The radiation and the conduction terms are typically orders of magnitude smaller than the parallel plasma heat flux and can be neglected during Alcator C plasma discharges. Therefore we can obtain the incident plasma heat flux by using:

$$q_{\|}(t) \sim \frac{\rho\, V_{plate}\, C_p}{A_{exp}} \frac{dT(t)}{dt}, \tag{2}$$

where V_{plate} is the volume of the calorimeter plate; A_{exp} is the exposed area to the incident plasma; and $T(t)$ is the time evolution of the measured calorimeter plate temperature.

The calorimeter measurement is prone to pick-up noise due to the changing ohmic and toroidal field coil currents, although typically the toroidal field magnet current is constant during the plasma discharge. In addition, if the plate is subjected to large fluctuating floating potentials, it is difficult for simple differential op-amp circuit to deduce the induced emf reading without extraordinarily high common mode rejection ratios.

2.3 Results

Figure 4 shows the electron side heat flux measurement for a high density, high current Alcator C discharge. As mentioned previously, the radiation loss and the conduction loss terms are small in comparison with the parallel plasma heat flux.

The $q_{\|}$ measurements have several sources of uncertainties. Some of them have been discussed in section 2.2. Another dominent source of uncertainties is the energy reflection coefficient. Since a large amount of particles are backscattered, carrying away a significant amount of energy, the $q_{\|}$ measured is only a portion of the total plasma heat flux. This effect must be considered as a correction. However few, if any, experimental measurements have been performed to determine the energy reflection coefficients. Most of the low energy data are obtained using computational models[24,25,26]. The actual energy reflection coefficient is a function of the incident particle energy, incident angle, and material properties. For normal incident deuterons on tungsten, the projected energy reflection coefficient is approximately 0.6. However, the calorimeter plate is also subjected to metallic deposition from the plasma, where the principle metallic impurities are molybdenum (limiter) and iron (vacuum vessel).

In a magnetized plasma the charged particles, on average, can strike the material surface at an oblique angle despite the presence of the sheath potential[27]. This effect would increase the overall energy reflection coefficient[26,27].

Compared to other candidate high heat flux materials tungsten has a very large energy reflection coefficient. To obtain a larger temperature rise corresponding to an incident heat flux, future calorimeter study should incorporate this reflection coefficient into the design guideline.

2.4 Implication: Sheath Transmission Coefficient

Provided all the contributing uncertainties can be correctly accounted, we can determine the total sheath transmission coefficient[28] by combining the $q_{||}$ measurements with the RFEA and Langmuir probe data. Typically the total heat flux is formulated as

$$q_{||} \quad = \quad \Gamma_{||}\, \kappa T_e\, \delta_t, \tag{3}$$

where $\Gamma_{||}$ is the incoming particle flux and δ_t is the sheath transmission coefficient. δ_t, when multiplied together with T_e, can be defined as the amount of energy deposited onto the incident material surface by an ion-electron pair. It is a complicated function consisting of contributions from the ion and electron energies, the local sheath potential, secondary electron emission, and the material properties.

Janus is capable of measuring all the parameters in equation 3 in order to solve for δ_t. $\Gamma_{||}$ and T_e are obtained from standard Langmuir probe analysis (section 4) and $q_{||}$ from the calorimeter. For the shot corresponding to figure 4, we obtained $\delta_t^{measured} \sim 2.5$ by assuming a reflection coefficient of 0.5. This is lower than the theoretically predicted δ_t by a factor of 2.5. The difference could be due to incorrect theory or by the uncertainties in the $q_{||}$ measurement mentioned earlier.

3. Retarding Field Energy Analyzer

Few edge plasma diagnostics are capable of measuring the ion parameters directly. A sample of those used previously are surface probes[29,30], $E \times B$ probes[31,32], aperture transmission probes[33], Katsumata probes[34], biased heat flux probes[35], carbon resistance probes[36], and retarding field energy analyzers (RFEA)[32,37,38,39]. Matthews[39] gives an excellent review on these diagnostics, both the principles and the usefulness for fusion plasma applications. The retarding field energy analyzer is assessed to be the best overall ion parameter diagnostic for its versatility and reliability.

3.1 Design Consideration

The RFEA is a versatile edge diagnostic designed to measure the parallel ion or electron energy distribution functions. Previously, different versions of the RFEA have been used successfully in various fusion devices for different purposes[32,37,38,39]. An excellent review on the design principles of the RFEA is given by Molvik[38].

Figure 3 shows a cross-sectional view of the RFEA used for Janus. It consists of 5 components: a knife-edge slit, 3 double-sided mesh electrodes, and a collector. As sketched in figure 2, all components rest in Al_2O_3 insulators and are pressed together using a flat, U-shaped, stainless steel spring.

The knife-edge slit is the most difficult component of RFEA to design and manufacture. The slit opening at the plasma side must be less than twice the sheath thickness, δ_{sheath}, in order to assure the continuity of the sheath potential surface across the front of the probe. This design constraint assures that the charged particle distribution functions are not perturbed by a uneven distribution of the sheath potential. Theoretically δ_{sheath} is characterized as[39,40,41]:

$$\delta_{sheath} \leq 10\ \lambda_{Debye}, \tag{4}$$

$$\text{where } \lambda_{Debye} = 743\sqrt{\frac{T_e}{n}}\ \text{(cm)}. \tag{5}$$

Here T_e is the electron temperature in eV and n is the plasma density in cm^{-3}. Applying typical Alcator C edge conditions of $T_e \sim 15$ eV and n $\sim 1\times10^{13}$ cm^{-3}, we obtain $\lambda_{Debye} \sim 9\mu\text{m}$. The RFEA slits for Janus are designed with a width of 30 μm. The slits are made of 0.635 mm thick tungsten plates, similar to the calorimeters, so that the slits can absorb a high heat flux without the danger of melting. Each slit is comprised of two half pieces which are "carved" out of the tungsten plate by using wire EDM processes. The knife-edges are machined by using conventional EDM processes and a notch besides the knife-edge defines the slit width. The two half pieces are welded together by electron beam.

In a magnetized plasma, the ions gyrate about magnetic field lines with a gyroradius ρ_i, which is defined as:

$$\rho_i \;=\; 1.02 \times 10^2 \; \frac{\sqrt{\mu T_i}}{Z B} \quad (\mathrm{cm}), \tag{6}$$

where μ is the mass (in amu) of the charged particle with charge Z; T_i is the perpendicular ion temperature in eV; and B is the magnetic field in Tesla. For hydrogen ions at 8 Tesla and 25 eV, $\rho_i \sim 60\ \mu\mathrm{m}$, which is larger than the designed slit width. A large fraction of ions with such large gyroradii can be scraped off as they pass through the slit, never reaching the RFEA chamber. To minimize this effect, the slit is designed like a knife edge. In this way, as soon as an ion enters the slit the overall aperture for transmission is enlarged. The transmission properties of various slit geometries are studied using a Monte-Carlo ion orbit code. Results of such study for Janus indicate that although the slit reduces the transmission, it does not perturb the parallel energy distribution of the incoming charged particles.

The electrodes employ a doubled-sided mesh design[42] to avoid potential shielding by the electrons inside the analyzer and to avoid the field penetration effect from adjacent electrodes. The mesh spacing is chosen based on the estimated electron density inside the analyzer chamber. Therefore the mesh closest to the slit faces the most stringent spacing requirement. It is also subjected to the largest heat flux and may be damaged by melting. For the Janus design, the first electrode employs 250 lines/inch tungsten meshes with a line weight of 0.001 inch. The rest of the electrodes use 150 lines/inch tungsten meshes with similar line weight.

The separation between the 2 meshes within the same electrode are chosen to avoid the existance of Móire fringes[38]. Thus the transmission characteristic of each mesh is independent of the characteristics of the other meshes. The transmission is in general a function of the component geometry, the particle energetics, the applied potential, and magnetic field. For simplicity of calculation, these effects are estimated by using the Monte-Carlo code previously mentioned.

Each transmission coefficient is found to be nearly independent of the particle energetics and the applied potential. It is important that the individual transmission characteristics be very weak functions of the particle parallel energy in order to unambiguously unfold the parallel energy distribution function. The overall transmission coefficient, T_T, is just the multiple of all the individual component transmission coefficients, T_j:

$$T_T \quad = \quad \prod_{j=1}^{n} T_j. \tag{7}$$

Here T_j's designate the contributions of the slit and meshes.

In the absence of a magnetic field, the maximum allowed incoming current density due to space charge limitation, J_{max}, is determined by the analyzer's biasing scheme and the electrode separation[38,43]. This would pose a severe limitation upon the operating limit of the RFEA. However within the high magnetic field of Alcator C the charged particles observe Brillouin flow[32,39,44]. The maximum current density that can be carried without divergence in this case is given by

$$J_{max} \quad = \quad 5.86 \times 10^{-4} \; \mu^{-1.5} \; B^2 \; \Phi^{0.5} \quad (\mathrm{Amps/cm^2}), \tag{8}$$

where Φ is the averaged beam energy in eV.

The space charge limit can be investigated experimentally by studying the dependence of the collected current as a function of the biased voltage. By sweeping the bias voltage up and down, for example using a triangular sweep, if the space charge limit is violated, the collected current will exhibit a hysterisis pattern instead of retracing the same pattern during ramp-up and ramp-down[42]. Successive traces can be overlapped to examine the space charge effects. Thus far there is no apparent violation of the space charge limitation within the operating regime of Janus.

Other design considerations include the possible lens effect that would occur if the mesh openings were large compared to grid separation distance and possible neutral density build-up within the analyzer. The former is a minor effect for our operating regime. The latter is taken account in the design by providing a neutral pump-out passage just before the collector plate. Photoelectrons can also contribute to the total collector current. However, given the geometry of Alcator C, the high energy photon flux is insignificant.

3.2 RFEA Bias and Analysis Techniques

Provided that the slit design introduces negligible perturbations to both the electron and ion parallel energy distributions, the grid electrodes between the collector and the slit can be biased to collect integrated parallel energy distribution functions of the ions and electrons. In Janus, the first 2 grids are sufficient for RFEA operation. The third grid is used as an emergency backup in case the first grid is damaged and is usually electrically tied to the collector. The probe casing is grounded to the vacuum vessel at the access flange.

Using a LeCroy 8601 Complex Function Generator we can produce the complex waveforms shown in figure 5. The first grid (closest to the slit) always serves as the ion repeller. The second grid serves as the primary electron repeller as well as the secondary electron suppressor.

During the first part of the voltage sweep shown in figure 5(a), the analyzer is operating in *ion mode*. The first electrode is swept with a triangular waveform from a large positive potential to probe ground. The action of this grid is to repel away all ions with energies less than the applied electrode potential. Simultaneously the second electrode is held at a large negative potential to repel away all primary electrons and also to suppress the secondary electrons emitted from the collector.

Measurement of the electron distribution function (*electron mode*) starts after the first grid completes its triangular sweep in voltage. This part is labeled as (b) of figure 5. Now the first electrode is held at a very high positive potential to repel away all the primary ions. At the point when the first electrode potential levels off, the second electrode now starts to sweep from a large negative potential to probe ground and back. Thus all electrons with energies less than the second grid potential are repelled. Secondary electrons are still suppressed since during this sweep the collector is still at a more positive potential than the second grid.

The collected current is shown as solid circles in figure 5. It follows the behavior predicted by

$$I(V) \quad = \quad e \; A_{slit} \; T_T \quad \int_{qV}^{\infty} v_{\|} \, f(E_{\|}) \, dE_{\|}, \tag{9}$$

where e is the charge of the incoming particle, A_{slit} the total slit area, and V is the biasing potential of the primary retarding electrode. $v_{\|}$ and $E_{\|}$ are defined as the particle parallel velocity and parallel energy respectively. T_T is the total transmission coefficient calculated by equation 7. All particles possessing parallel energy, $E_{\|}$, larger than the biased potential, V, will be collected provided they are transmitted through all analyzer components.

To unfold the ion or electron parallel energy distribution function we can, in principle, take the numerical derivative of equation 9 and solve for $f(E_{\|})$ such that

$$f(E_{\|} = V) \quad = \quad \frac{-m}{e^2 \; A_{slit} \; T_T} \; \frac{dI(V)}{dV}, \tag{10}$$

where m is the mass of the charged particle. However $I(V)$ is typically noisy due to large edge density fluctuations and is therefore difficult to differentiate. A much more practical technique is to assume a form for $f(E_{||})$ and compare $I(V)$ obtained from equation 9 with the experimental data.

Kinetic theory[45] predicts that the ion distribution at the material surface approximates that of a Maxwellian with a positive energy shift corresponding to the sheath potential $|V_{sheath}|$. This is equal to the plasma potential, V_{plasma}, with respect to the probe ground. Therefore, from equation 9, the ion current as a function of the retarding potential V is

$$\begin{aligned} V \leq V_{sheath}, \qquad I_i(V) &= I_{oi}, \qquad \text{and} \\ V \geq V_{sheath}, \qquad I_i(V) &= I_{oi}\ \exp(\frac{-e(V - V_{sheath})}{kT_i}). \end{aligned} \tag{11}$$

I_{oi} is the ion current collected when none of the ions are repelled by the retarding potential. It is dependent on the density of the incoming species, its temperature, and the transmission characteristicss. If T_T can be estimated accurately, we can obtain an approximate ion density using the temperature implied by fitting equation 11. Typical fits to the ion part of the previously shown raw data (figure 5) are shown in figures 6(a) and 6(b). This data was taken with a 2 kHz 6-pole active Butterworth filter to reduce the fluctuation level. Residual oscillations under 2 kHz are still evident in this data.

Due to the formation of the sheath potential between the slit surface and the unperturbed plasma, the bulk of the electron distribution is repelled. Only the high energy portion of the electron distribution is collected. Again assuming a Maxwellian form for the electron distribution function, we can obtain a version of equation 11 for electrons:

$$I_e(V) = I_{oe}\ \exp(\frac{eV}{kT_e}), \tag{12}$$

where I_{oe} is the electron current at V = 0 volts. The electron density is more difficult to determine than the ions since accurate knowledge of V_{sheath} is necessary in order to determine the fraction of electrons repelled by the negative slit potential. Figures 6(c) and 6(d) show typical fits of the electron portions of the raw data in figure 5.

The assumption of Maxwellian distributions for both the ions and electrons are appropriate within the accuracy of the data. As demonstrated in figures 5 and 6, the ions follow a shifted Maxwellian distribution and the electrons appear to be a cut-off Maxwellian. The energy shift in the ion distribution should be equal to the potential difference between the unperturbed plasma and the entrance slit. Typically, the slit is grounded at the port where Janus is installed. Therefore this shift is a measurement of the local plasma potential with respect to the port potential.

One important issue here is the effect of a perturbing probe (Janus) on the measured plasma parameters. This effect has previously been addressed by Stangeby[20,21]. The insertion of a large, perturbing probe in the scrape-off layer creates new scrape-off lengths on both sides of Janus. Therefore the measured parameters are different than the natural, unperturbed plasma parameters. The relation of the perturbed parameters and the unperturbed parameters are dependent on the tokamak's limiter (or divertor) configuration and the probe geometry.

4 Langmuir Probe

Due to its simplicity and versatility, the Langmuir probe is the most frequently used edge plasma diagnostic. And depending on the operating and analysis techniques chosen, the Langmuir probe can measure a variety of plasma information including an independent measurement of T_e, plasma density, ion saturation current, floating potential, and fluctuation levels. Thus the Langmuir probe is an excellent complimentry diagnostic to the RFEA.

4.1 Design Consideration

The Langmuir probe on Janus is a single probe protruding from the housing. The probe consists of a cylindrical tip supported on a smaller diameter ceramic-insulated wire which makes the electrical connection back through the housing. The tip is also larger in diameter (along a field line) than the ceramic insulator covering the support wire in order to avoid metallic deposition onto the insulator which might cause an electrical connection of the probe to the Janus housing. The entire Langmuir probe is made of molybdenum and no melting was evident during the entire initial operating period of Janus.

4.2 Analysis Technique

The Langmuir probe analysis technique used for this high magnetic field application is well documented[46,47]. The Janus Langmuir probe surface is aligned perpendicular to magnetic field lines and the surface is large compared to ion gyroradii. The collection area is assumed to be planer. For our analysis we principally employed a simple probe theory and obtain T_e by fitting only the exponential portion of the probe characteristic [10,47]. However the main question here is the validity of the simple probe theory in a magnetized environment. A logarithmic fit as well as the theory of Stangeby[48] were also used for electron temperature analysis.

Two independent measurements of T_e are obtained using the RFEA and the Langmuir probe. Therefore, we can cross-check the T_e measurements and attempt to check the validity of the probe theory. Figure 7(a) shows typical T_e results obtained by these two diagnostics in Janus. The electron temperature measurement using an exponential fit to the Langmuir trace agreed with the independent measurement from the RFEA on the same Janus housing throughout the entire discharge. Thus we have confidence that the measurement of T_e through the exponential fit is valid. However, the same agreement was not found with the use of the Stangeby fit, which is typically lower than the exponential fitted T_e by 30% or more.

In order to obtain an approximate plasma density from the probe characteristic, we measure the ion saturation current, I_{sat}, and assume a sonic flow to the probe sheath edge:

$$I_{sat} \sim 0.5\, n_{\infty}\, C_s\, e\, A_p, \tag{13}$$

where n_{∞} is the unperturbed plasma density far away from the probe and A_p is the probe surface area. C_s is the sound speed which includes both the ion and electron temperatures.

Once again, the relationship between the Janus measurements and the unperturbed plasma parameters is unclear. As addressed in section 3, Stangeby's theory can be used to unfold the Janus measurements.

5. RFEA and Langmuir Probe Results

Figure 7 shows the results obtained by the RFEA and the Langmuir probe on the electron side of Janus. Figure 8 shows the ion side results. Each figure displays T_i and T_e as measured by the RFEA, as well as T_e, n_{∞}, and V_{float} as measured by the Langmuir probe. As previously mentioned, the two independent T_e measurements agree very well.

The results shown in figures 7 and 8 are taken for a line-averaged central density of $\sim 8 \times 10^{13}$ cm^{-3} and peak plasma current of 280 kA. Two phenomena which deserve full attention are the difference in T_i/T_e ratios, and the absolute values of temperatures and densities as measured on the ion and electron sides.

The temperature measurements on both sides of Janus indicate T_i/T_e ratios exceeding 1, suggesting energy decoupling between the edge ions and electrons. From minor radius scan data, we can conclude that this phenomenon is not an artifact of inserting a large, perturbing probe in the scrape-off layer (SOL) since the measured ion and electron temperature scrape-off lengths are approximately the same. Thus T_i and T_e difference can not be attributed to different perpendicular transport mechanisms for ions and electrons (to the diagnostic sensors recessed back by 0.5 cm from the edge of the probe casing). Therefore each specie is dominated by different energy loss or gain mechanisms. Using the measured edge parameters we have calculated the electron-ion energy equipartition time scale, τ_{ei}, which is found to be much longer than time scales of other possible mechanisms, such as parallel convection and charge exchange.

Janus is not the first Alcator C diagnostic to observe the ion side/electron side asymmetries. Looking at the limiter damage pattern alone we noticed melting occuring at the top inside on the electron side and bottom inside on the ion side[10,49]. A thermocouple array imbedded in limiter blocks also yielded similar results[50].

As can be seen in figures 7 and 8, measured plasma parameters are not symmetric with respect to the two Janus viewing directions. The asymmetry pattern always favors larger temperatures and densities on the electron side as the toroidal field is oriented anti-parallel with respect to the plasma current. However, as we reverse $B_{toroidal}$ the asymmetry pattern also changes. In the reverse field configuration, as Janus is pushed closer to the limiter radius, the ion side parameters increase until they eventually dominate over the electron side parameters. For normal field configuration the ratios of electron side/ion side densities and temperatures become larger as Janus approaches the limiter radius. Physics implication behind this directional asymmetry is beyond the scope of this paper and will be discussed in later publications.

6. Summary

Janus is designed to measure most of the relevant edge parameters simultaneously along both directions of a field line. On each side of Janus there is an identical set of three diagnostics, a Langmuir probe, a calorimeter and a retarding-field energy analyzer. It is designed to be a localized diagnostic, avoiding the uncertainty of measuring different edge parameters in a poloidally asymmetric edge plasma.

The calorimeter is designed to measure the total parallel heat flux incident onto an electrically floating plate. Uncertainties due to energy reflection coefficient and 3-D thermal transport effect need to be resolved in order to accurately measure the total parallel heat flux.

The retarding field energy analyzer measures the parallel energy distributions of the ions and electrons. Both distribution functions follow closely the expected Maxwellian form. From these distributions, values of the ion and electron temperatures can be inferred. An energy shift in the integrated ion current corresponds to the potential difference between the unperturbed plasma and the RFEA entrance slit. Density measurements are difficult to obtain due to uncertainties in the particle transmission coefficients at the grids.

The Langmuir probe measures the electron temperature, density, plasma floating potential, and fluctuation levels. The electron temperature is obtained by using a simple probe theory which fits only the exponential portion of the probe characteristic. T_e obtained by this Langmuir probe analysis agrees well with the value obtained by the RFEA.

Using Janus we can conduct a detailed, localized characterization of the plasma in the scrape-off layer. Preliminary results suggest ion and electron energy decoupling at the edge. Ion and electron temperatures and densities differ between the ion and electron sides. This side to side difference is found to be dependent on the orientation of the toroidal magnetic field direction with respect to the plasma current. Detailed physics implications of these edge phenomena will be presented in future studies.

Acknowledgments

The authors would like to thank Bob Childs for his assistance during various design phases. We would also like to acknowledge the support of the Alcator C group during this set of experiments. This work was supported by the U. S. Department of Energy Contract No. DE-AC02-78ET-51013.

References

[1] F. Wagner, M. Keilhacker, and the ASDEX and NI Teams, *J. Nucl. Mat.* **121**, 103–113 (1984) .

[2] M. Nagami, M. Kasai, A. Kitsunezaki, T. Kobayashi, S. Konoshima, T. Matsuda, N. Miya, H. Ninomiya, M. Shimada, H. Yokomizo, T. Angel, C. Armentrout, F. Blau, G. Bramson, N. Brooks, R. Chase, A. Colleraine, E. Fairbanks, J. Fasolo, R. Groebner, T. Hino, R. Hong, G. Jahns, J. Kamperschroer, J. Kim, A. Lieber, J. Lohr, D. McColl, L. Rottler, R. Seraydarian, R. Silagi, J. Smith, R. Snider, T. S. Taylor, J. Tooker, D. Vaslow, S. Wojtowicz, *Nuclear Fusion* **24**, 183 (1984).

[3] S. M. Kaye, M. G. Bell, K. Bol, D. Boyd, K. Brau, D. Buchenauer, R. Budny, A. Cavallo, P. Couture, T. Crowley, D. S. Darrow, H. Eubank, R. J. Fonck, R. Goldston, B. Grek, K. P. Jaehnig, D. Johnson, R. Kaita, H. Kugel, B. LeBlanc, J. Manickam, D. Manos, D. Mansfield, E. Mazzucato, R. McCann, D. McCune, K. McGuire, D. Mueller, A. Murdock, M. Okabayashi, K. Okano, D. K. Owens, D. E. Post, M. Reusch, G. L. Schmidt, S. Sesnic, R. Slusher, S. Suckewer, C. Surko, H. Takahashi, F. Tenney, H. Towner, J. Valley, *J. Nucl. Mat.* **121**, 115–125 (1984) .

[4] B. Lipschultz, B. LaBombard, E. S. Marmer, M. M. Pickrell, J. L. Terry, R. Watterson, S. M. Wolfe, *Nucl. Fusion* **24**, 977 (1984).

[5] F. P. Boody, C. E. Bush, S. S. Medley, H. Park, J. Schivell, *Bull. Amer. Phys. Soc.* **30**, paper 6P7, 1518 (Nov 1985).

[6] B. Lipschultz, B. LaBombard, H. L. Manning, J. L. Terry, S. Knowlton, E. S. Marmer, M. Porkolab, J. Rice, Y. Takase, S. Texter, A. Wan, M.I.T. Plasma Fusion Center Report PFC/JA-85-45 (Dec. 1985).

[7] G. M. McCracken, P. E. Stott, *Nucl. Fusion*, **19**, 889 (1979).

[8] D. M. Manos, G. M. McCracken, Proceedings of NATO Advanced Study Institute on Plasma Surface Interactions, Val Morin P.Q., Canada (August 1984).

[9] S. A. Cohen, Proceedings of IEEE Int'l. Conf. on Plasma Science, Montreal, Canada (1979).

[10] B. LaBombard, M.I.T. Doctoral Thesis.

[11] K. W. Gentle, C. C. Klepper, W. L. Rowan, *Bull. Amer. Phys. Soc.* **30**, paper 7R10 1567 (Nov 1985).

[12] P. C. Stangeby, G. M. McCracken, S. K. Erents, G. Matthews, *J. Vac. Sci. Technol. A* **2**, 702 (1984).

[13] S. J. Zweben, R. J. Taylor, *Nucl. Fusion* **23**, 513 (1983).

[14] A. S. Wan, B. Lipschultz, T. Yang, B. LaBombard, *Bull. Amer. Phys. Soc.* **30**, paper 3F6, 1413 (Nov 1985).

[15] S. Knowlton, S. McDermott, M. Porkolab, Y. Takase, S. Texter, P. Bonoli, C. Fiore, S. McCool, M. Mayberry, K. I. Chen, S. C. Luckhardt, R. Rohatgi, Proceedings of the 11th Int'l. Conf. on Plasma Physics and Controlled Nucl. Fusion Research, Budapast, Hungary (Sept 1985).

[16] M. Porkalab, B. Blackwell, P. Bonoli, D. Griffin, S. Knowlton, B. Lloyd, J. Moody, J. J. Schuss, Y. Takase, S. Texter, R. Watterson, C. Fiore, M. Foord, R. Gandy, C. Gomez, R. Granetz, M. Greenwald, D. Gwinn, B. LaBombard, B. Lipschultz, H. Manning, E. Marmer, S. McCool, J. Moreno, A. Pachtman, D. Pappas, R. Parker, P. Pribyl, J. Rice, T. Shepard, J. Terry, S. Wolfe, D. Yates, K. I. Chen, S. C. Luckhardt, M. J. Mayberry, G. Bekefi, R. Rohatgi, Proceedings of the 10th Int'l. Conf. on Plasma Physics and Controlled Nucl. Fusion Research, London (Sept 1984).

[17] M. Greenwald, D. Gwinn, S. Milora, J. Parker, R. Parker, S. Wolfe, and Alcator Group, *Phys. Rev. Let.* **53**, 352 (1984).

[18] J. L. Terry, R. S. Granetz, M. J. Greenwald, H. L. Manning, E. S. Marmer, M. Foord, C. Gomez, *Bull. Amer. Phys. Soc.* **30**, paper 3F3, 1413 (Nov 1985).

[19] E. S. Marmer, J. E. Rice, J. L. Terry, F. H. Seguin, *Nucl. Fusion* **22**, 1567 (1982) .

[20] P. C. Stangeby, *J. Nucl. Mat.* **121**, 36–40 (1984).

[21] P. C. Stangeby, *J. Phys. D: Appl. Phys.* **18**, 1547–1559 (1985) .

[22] Handbook of Heat Transfer, Editors: W. M. Rohsenow and J. P. Hartnett, McGraw-Hill, New York (1973).

[23] D. M. Manos, R. Budny, T. Satake, S. A. Cohen, *J. Nucl. Mat.* **111 & 112**, 130–136 (1982).

[24] W. Eckstein, H. Verbeek, *Max-Planck Institute Report IPP 9/32* August 1979.

[25] R. Ito, T. Tabata, N. Itoh, K. Morita, T. Kato, H. Tawara, Institute of Plasma Physics (Nagoya University) Report No. IPPJ-AM-41.

[26] T. Tabata, R. Ito, Y. Itikawa, N. Itoh; K. Morita, H. Tawara, Institute of Plasma Physics (Nagoya University) Report No. IPPJ-AM-34.

[27] R. J. Knize, *Nucl. Fusion* **25**, 1498 (1985).

[28] P. C. Stangeby, *Phys. Fluids* **27**, 682 (1984).

[29] S. Cohen, *J. Nucl. Mat.* **76 & 77**, 68–77 (1978).

[30] G. Staudenmaier, P. Staib, R. Behrish, *Nucl. Fusion* **20**, 96 (1980).

[31] P. Staib, *J. Nucl. Mat.* **93 & 94**, 351–356 (1980).

[32] G. F. Matthews, *J. Phys. D: Appl. Phys.* **17**, 2243–2254 (1984).

[33] G. Staudenmaier, P. Staib, W. Porschenrieder, *J. Nucl. Mat.* **93 & 94**, 121–126 (1980).

[34] I. Katsumata, M. Okazaki, *Jap. J. Appl. Phys.* **6**, 123 (1967).

[35] P. C. Stangeby, G. M. McCracken, S. K. Erents, J. E. Vince, R. Wilden, *J. Vac. Sci. Technol. A* **1**, 1302 (1983).

[36] W. R. Wampler, D. M. Manos, *J. Vac. Sci. and Technol.* **1** (2) Part 2, 827 (1983).

[37] H. Kimura, H. Maeda, N. Ueda, M. Seki, H. Kawamura, S. Yamamoto, M. Nagami, K. Odajima, S. Sengoku, Y. Shimomura, it Nucl. Fusion **18**, 1195 (1978).

[38] A. W. Molvik, *The Rev. of Sci. Inst.* **52**, 704 (1981).

[39] G. F. Matthews, Oxford Doctoral Thesis.

[40] L. Tonks, I. Langmuir, *Phys. Rev.* **34**, (Sept 1929).

[41] S. A. Self, *Phys. of Fluids* **6**, 1762 (1963).

[42] S. Stephanakis, W. H. Bennett, *The Rev. of Sci. Inst.* **39**, 1714 (1968).

[43] I. Langmuir, K. T. Compton, *Rev. Mod. Phys.* **3**, 244 (1931).

[44] L. Brillouin, *Phys. Rev.* **67**, 260 (1945).

[45] G. A. Emmert, R. M. Wieland, T. A. Mense, J. N. Davidson, *Phys. Fluids* **24**, 803 (1980)

[46] F. F. Chen, "Electric Probes", Chapter 3 in Plasma Diagnostic Techniques, Editors: R. H. Huddlestone, and S. L. Leonard, Academic Press, New York (1965).

[47] B. Lipschultz, I. Hutchinson, B. LaBombard, A. Wan. M.I.T. Plasma Fusion Center Report PFC/JA-85-29 (Aug. 1985).

[48] P. C. Stangeby, *J. Phys. D: Appl. Phys.* **15**, 1007–1029 (1982).

[49] B. LaBombard, B. Lipschultz, I. Hutchinson, A. Wan, *Bull. Amer. Phys. Soc.* **30**, paper 3F7, 1413 (Nov. 1985).

[50] A. J. Hayzen, D. O. Overskei, J. Moreno, M.I.T. Plasma Fusion Center Report No. PFC/JA-81-10 (April 1981).

Table 1.1 - Alcator C Parameters

Alcator C Parameters	Standard Values	Range of Values
R_{major}	64 cm	57 – 71 cm
r_{minor}	16.5 cm	10 – 16.5 cm
$B_{toroidal}$	8 Tesla	5.5 – 13 Tesla
I_p	400 kA	100 – 700 kA
$n_e(central)$	2×10^{14} cm^{-3}	0.1 – 20. $\times 10^{14}$ cm^{-3}
T_e	1500 eV	1000 – 3000 eV
T_i	1100 eV	500 – 2000 eV

Figure Captions

[Figure 1.] Unscaled artist's conception of the Janus experimental set-up looking perpendicular to Janus' "viewing" length along a field line. Janus is situated between two full poloidal ring limiters with its ion side (as defined by I_p) having a shorter connection length.

[Figure 2.] 3-D view of a set of diagnostics on a single side of Janus. A mirror image set of diagnostics is on the other end with a U-shape flat spring inserted between the two sets to secure all components within the Janus housing. The Langmuir probe fits within the Al_2O_3 insulators of the RFEA.

[Figure 3.] Cross-sectional view of a RFEA. Components include a $30\mu m$ knife-edge slit, 3 double-sided mesh electrodes, and a collector. The connection between the wires originating from the probe head and the wires from the vacuum feedthrough are achieved using Be-Cu spring electrodes confined by carefully machined matching slot insulators, thus making the probe head detachable.

[Figure 4.] Measured temperature evolution (a) of the electron side calorimeter plate as a function of time. The deduced heat flux components that contributes toward the temperature rise are shown in part (b). The radiation loss and the conduction loss terms are orders of magnitude lower than the parallel plasma heat flux during the plasma discharge.

[Figure 5.] Bipolar operating mode of the RFEA. The solid line shows the bias waveform of the first grid and the dashed line shows the waveform of the second grid. The collected current is shown as solid circles. Region (a) of the figure shows the *ion mode* operation with the first grid ramping up and down to collected an integrated ion distribution as a function of the applied potential. All electrons are repelled away by a constant high negative potential of the second grid. In region (b), the *electron mode*, all ions are repelled by a constant high positive potential. The integrated electron distribution is obtained by ramping the second grid.

[Figure 6.] Fits corresponding to the raw data of figure 5. Parts (a) and (b) are the *ion* fits. The flat portions indicate the amount of energy shifts of the ion distributions which correspond to the potential difference between the entrance slit and the unperturbed plasma potential. The tail portions decay exponentially. Parts (c) and (d) are the *electron* fits. No energy shift is evident. The tails also decay exponentially.

[Figure 7.] Time histories of the electron-side edge parameters as measured by the Janus Langmuir probe and RFEA. Part (a) shows the ion and electron temperatures measured by the RFEA and the electron temperature measured by the Langmuir probe Both T_e's agree well with each other. Part (b) shows the plasma density as deduced by the Langmuir probe. Part (c) shows the plasma floating potential measured by the Langmuir probe.

[Figure 8.] Time histories of the ion-side edge parameters as measured by the Janus Langmuir probe and RFEA. Representations of the traces in parts (a), (b), and (c) are exactly the same as Figure 7. Once again, T_e agreements are excellent.

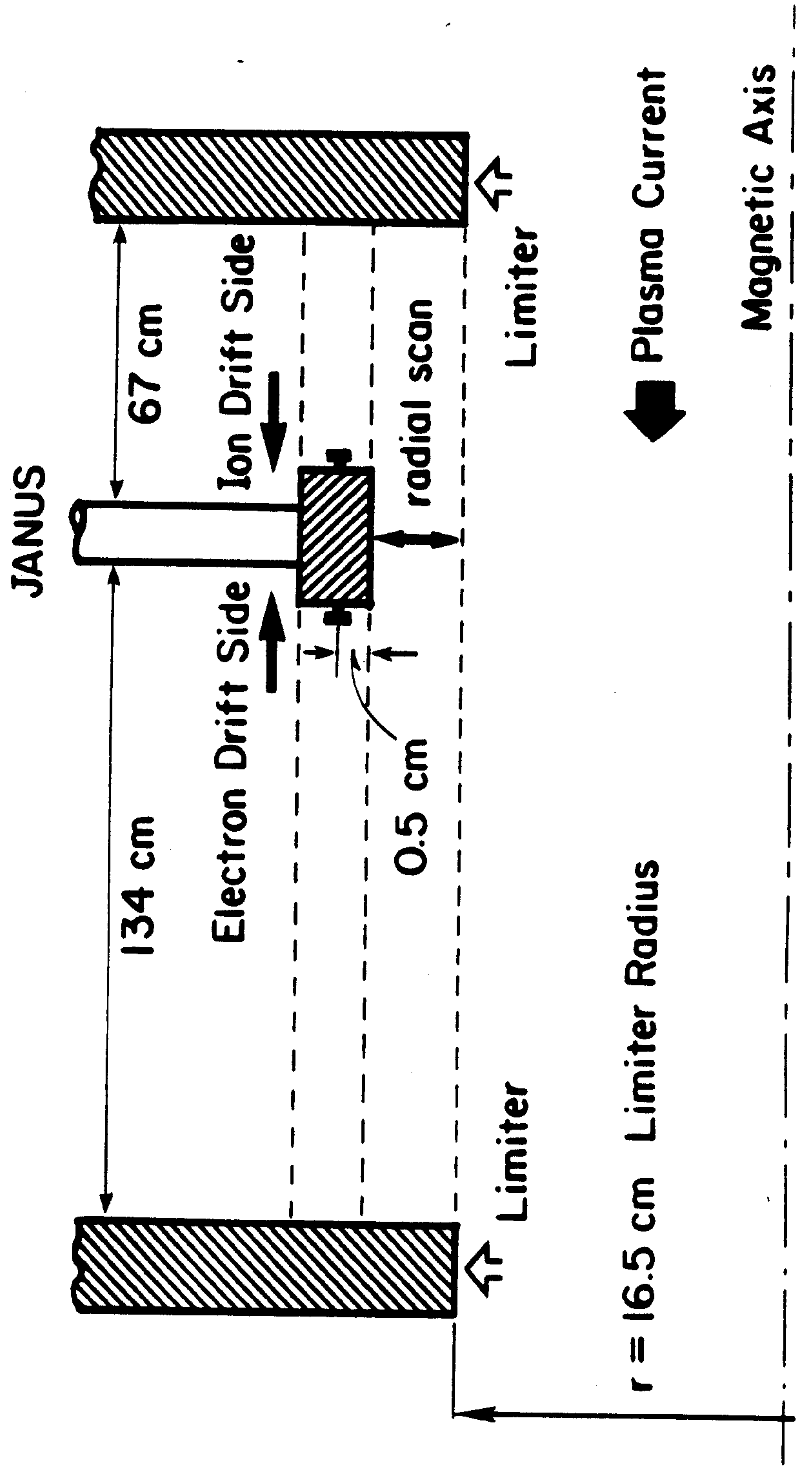
JANUS
67 cm
134 cm
Ion Drift Side
Electron Drift Side
radial scan
0.5 cm
Limiter
Limiter
Plasma Current
r = 16.5 cm Limiter Radius
Magnetic Axis

Figure 1

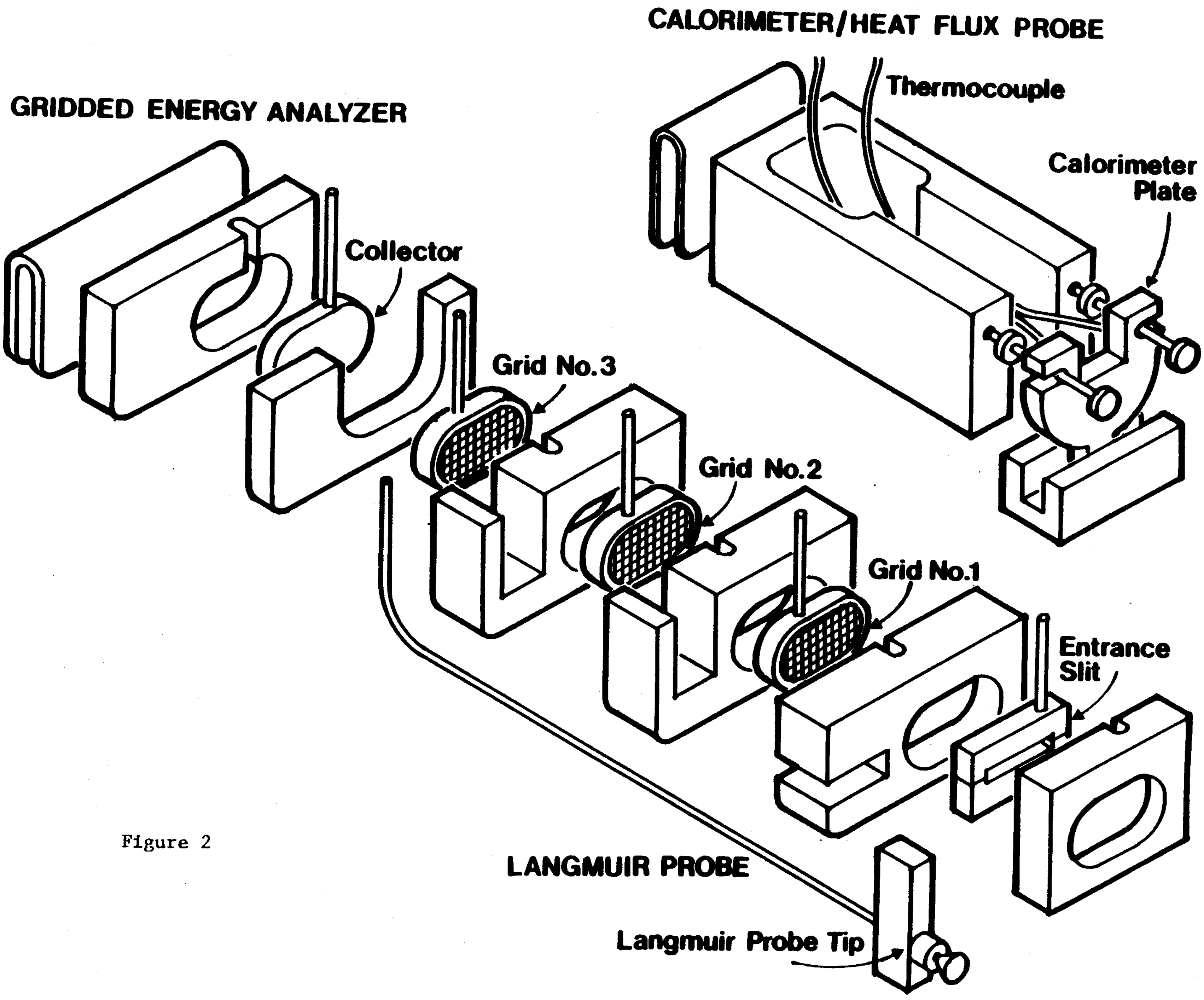
CALORIMETER/HEAT FLUX PROBE
Thermocouple
Calorimeter Plate
GRIDDED ENERGY ANALYZER
Collector
Grid No.3
Grid No.2
Grid No.1
Entrance Slit
LANGMUIR PROBE
Langmuir Probe Tip

Figure 2

8099/14/

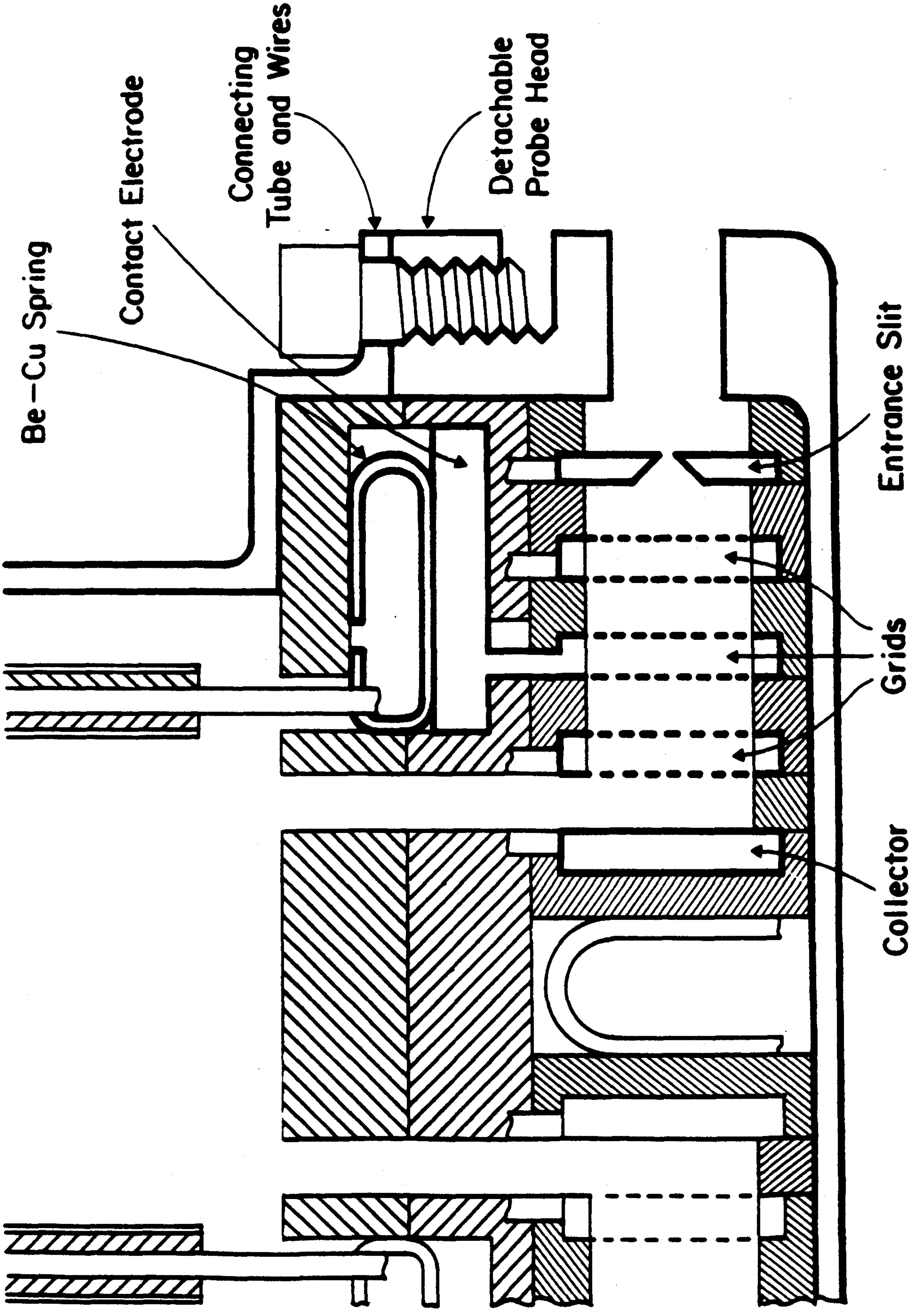

Figure 3

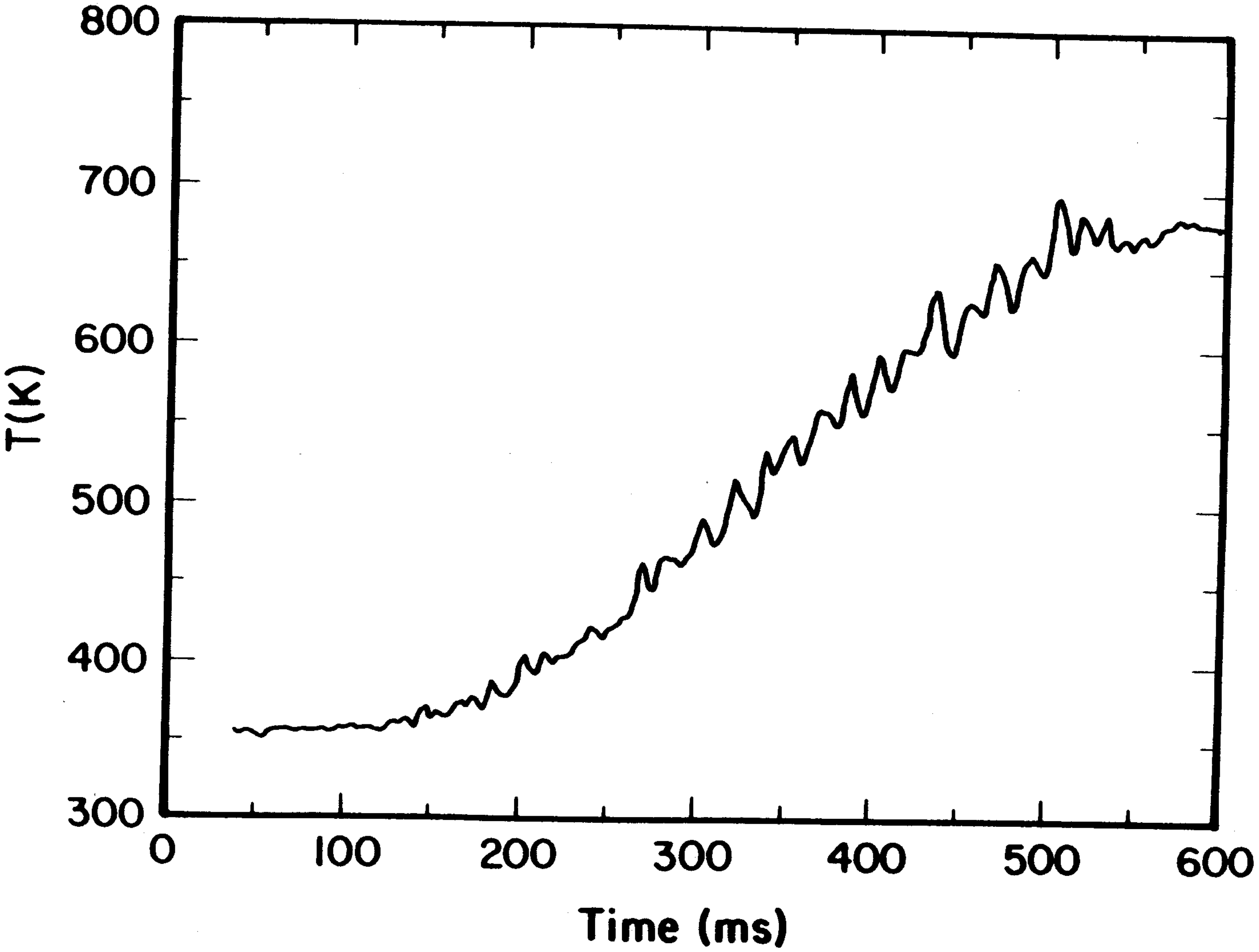

Figure 4(a)

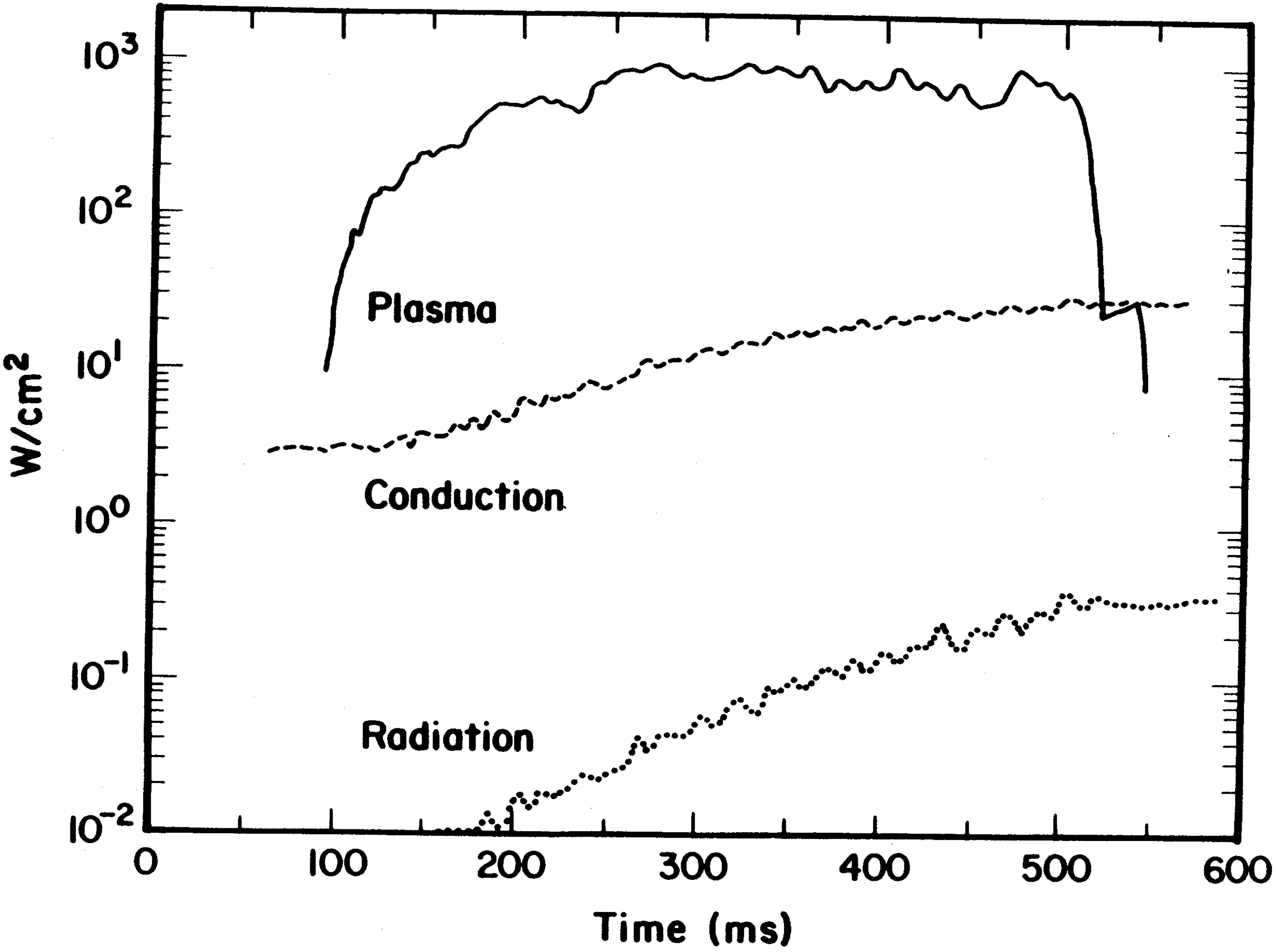
10^3
10^2
10^1
10^0
10^-1
10^-2
W/cm^2
Plasma
Conduction
Radiation
0
100
200
300
400
500
600
Time (ms)

Figure 4(b)

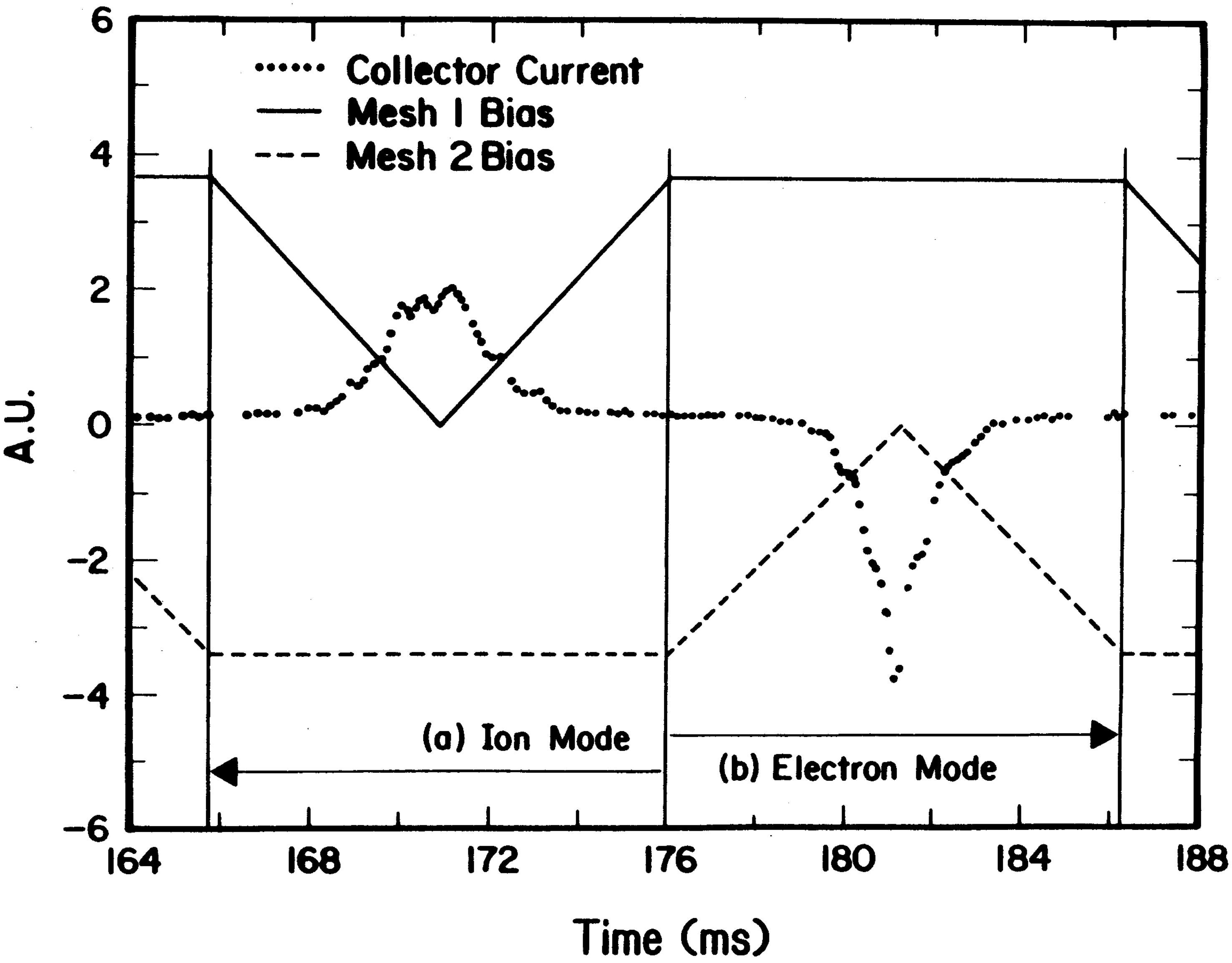

Figure 5

8099/14/13

Ion Mode

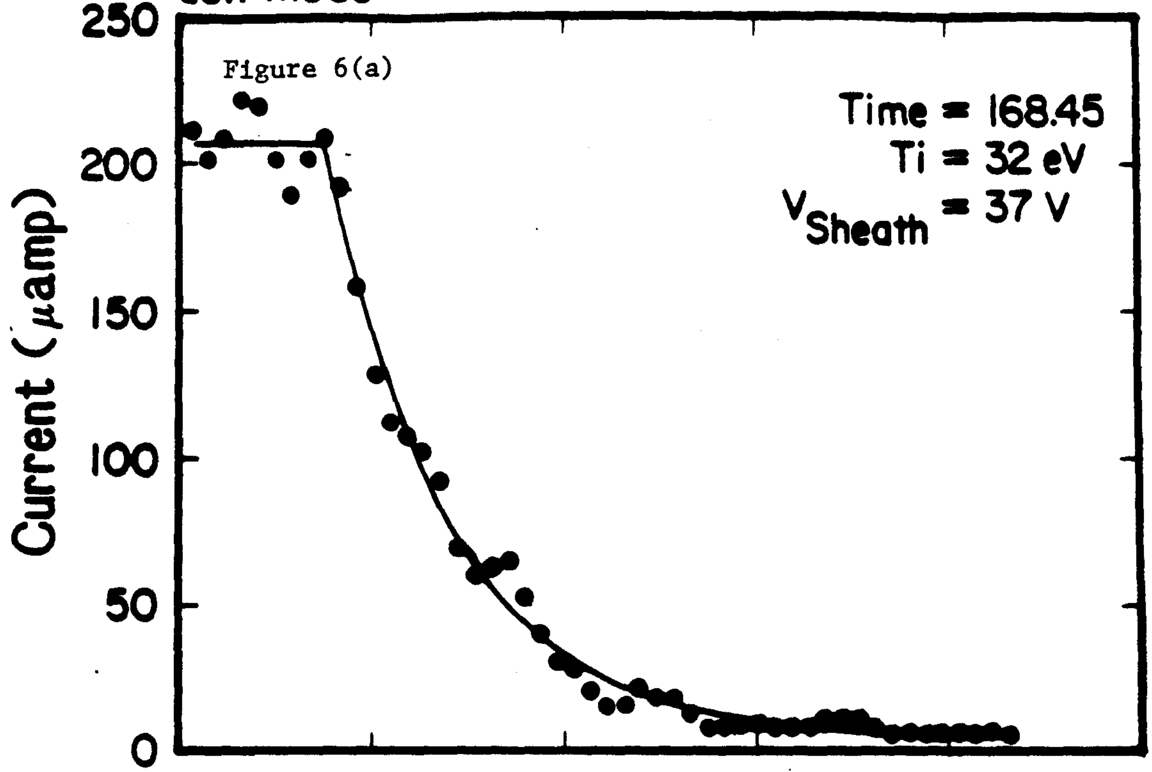

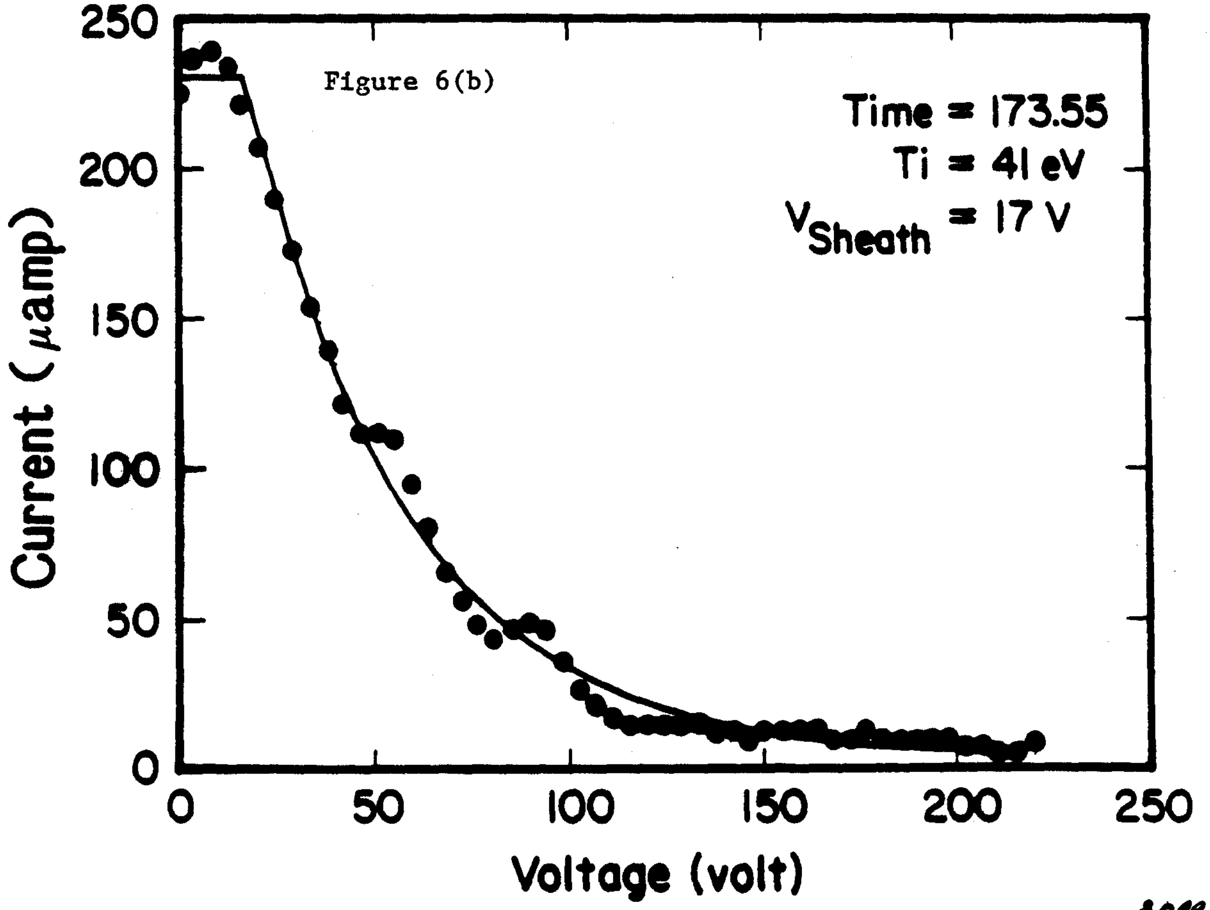

8099/14/14

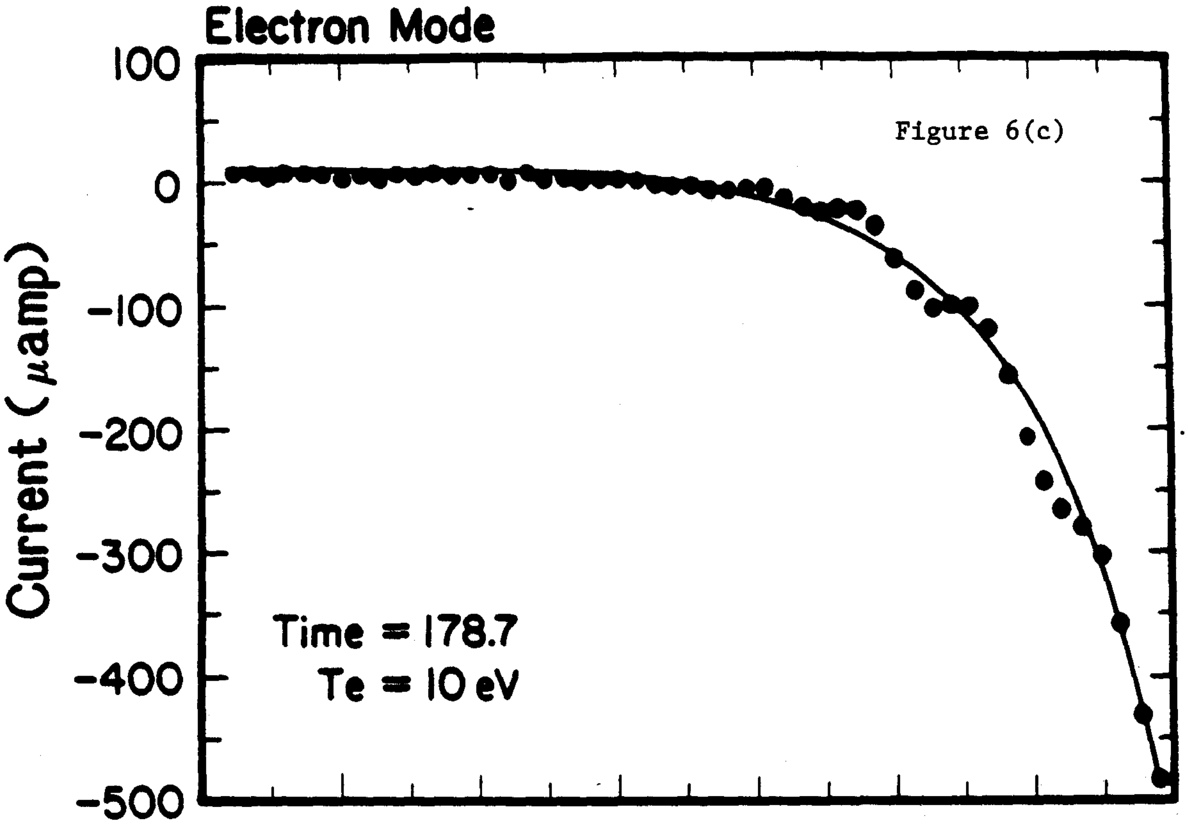

Figure 6(c)

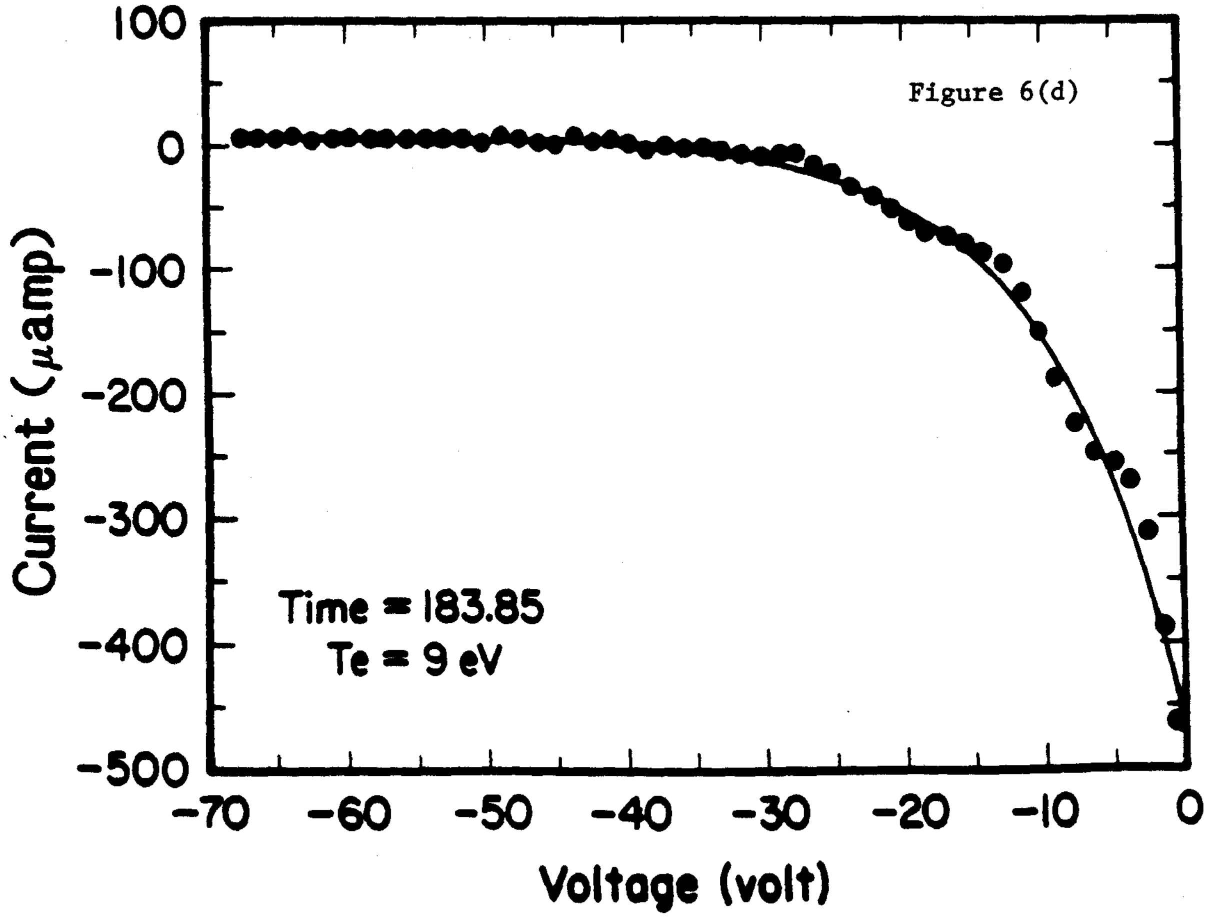

Figure 6(d)

8099/14/5

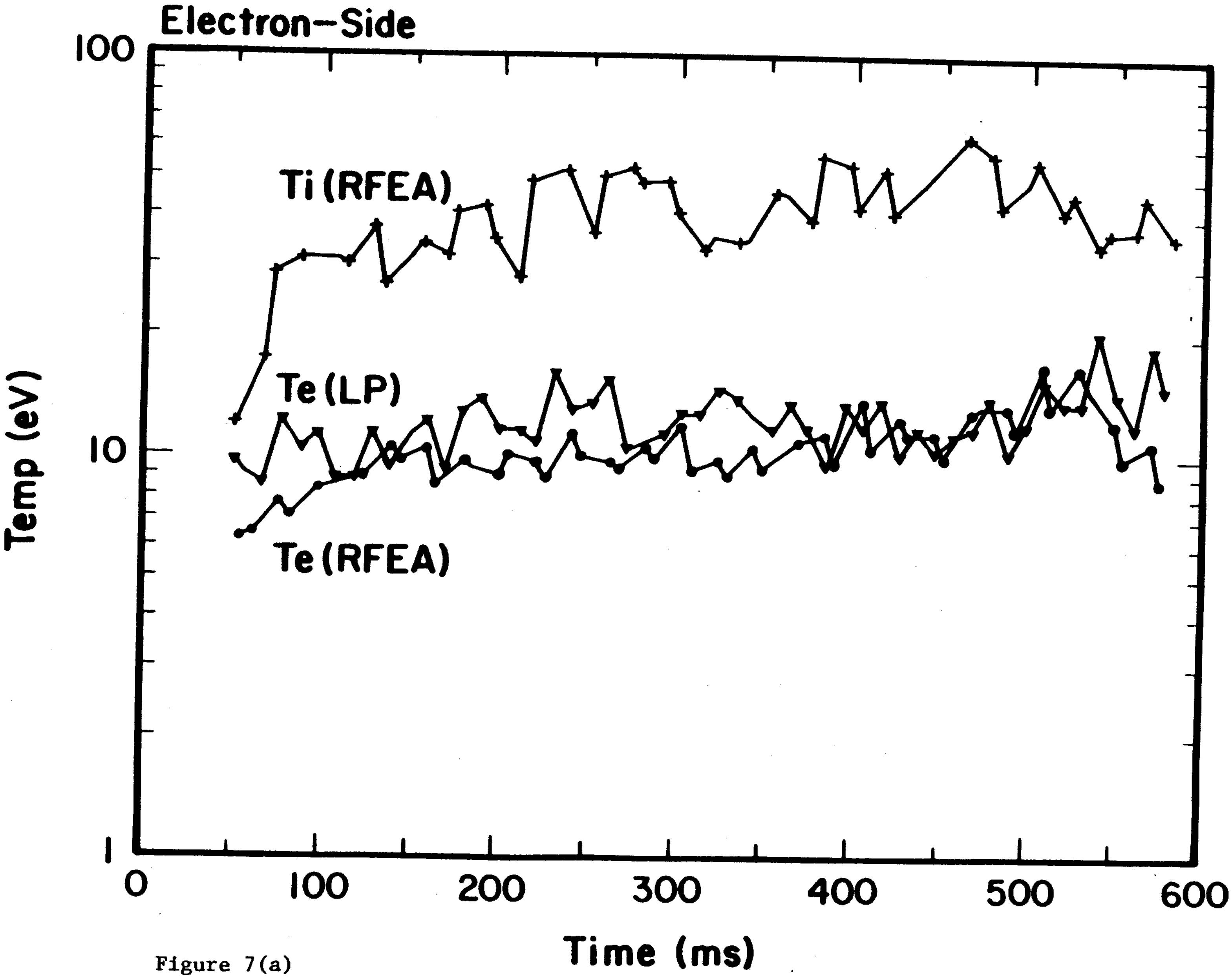

Figure 7(a)

8099/14/8

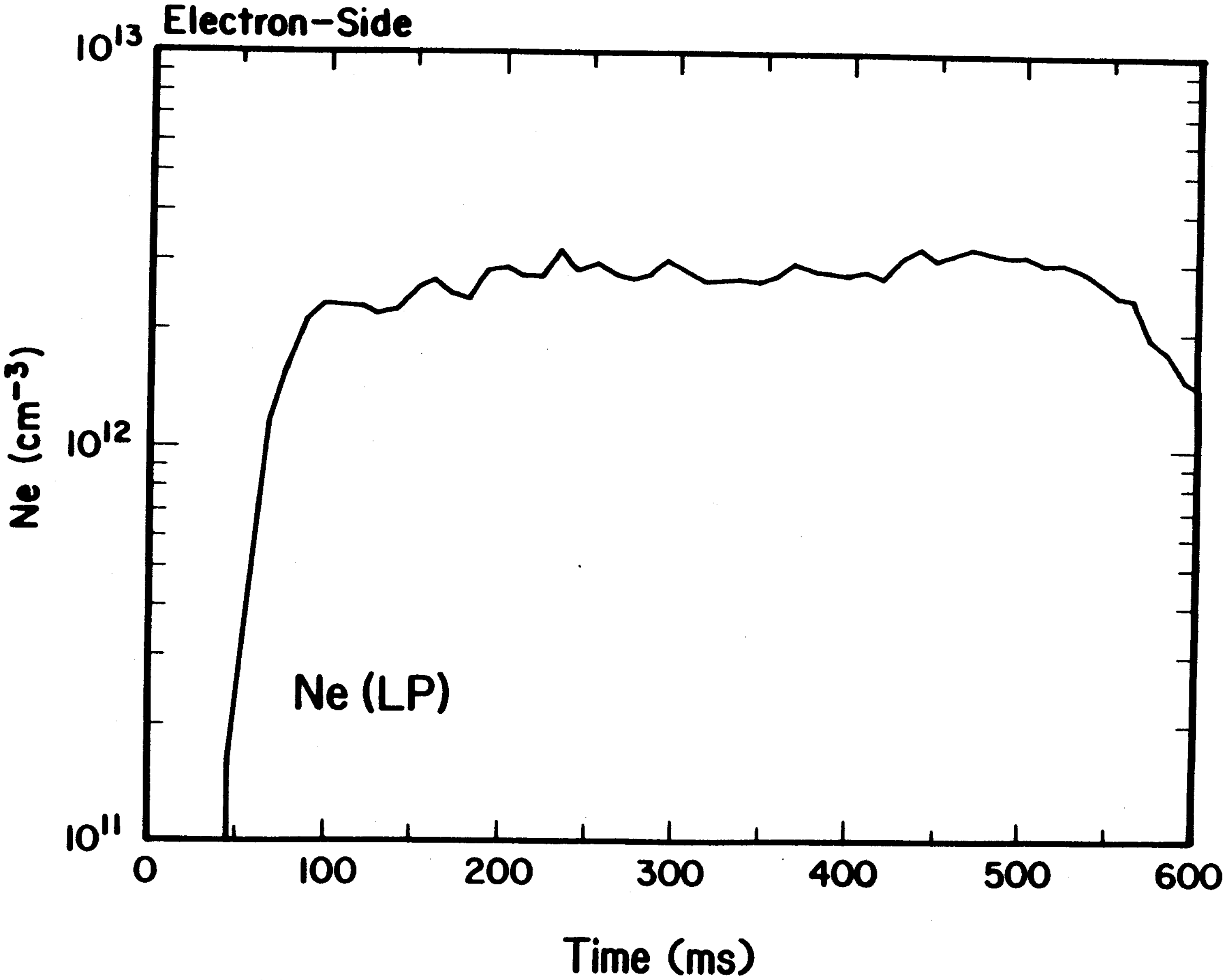

Figure 7(b)

8099/14/2

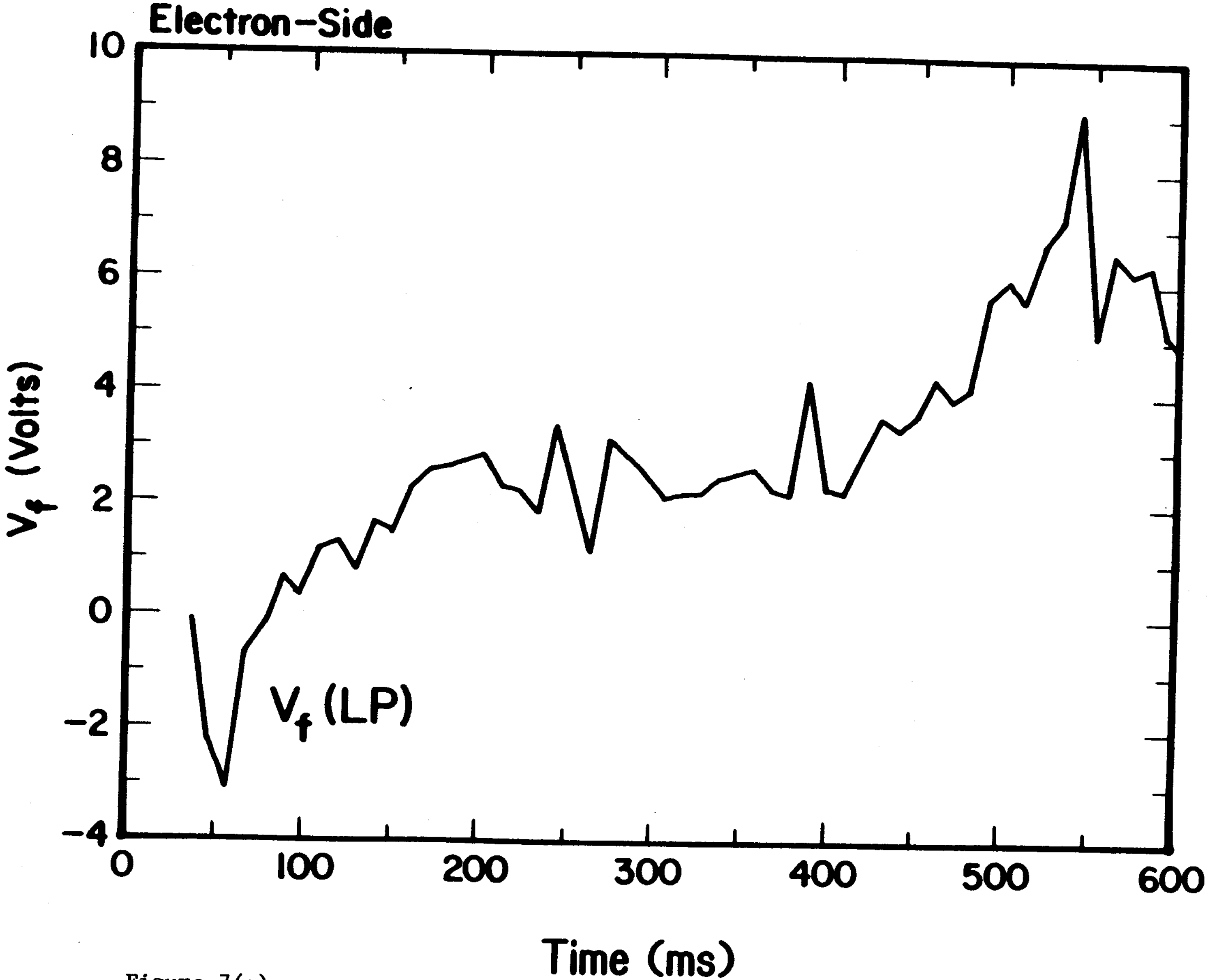

Figure 7(c)

0077/14/1

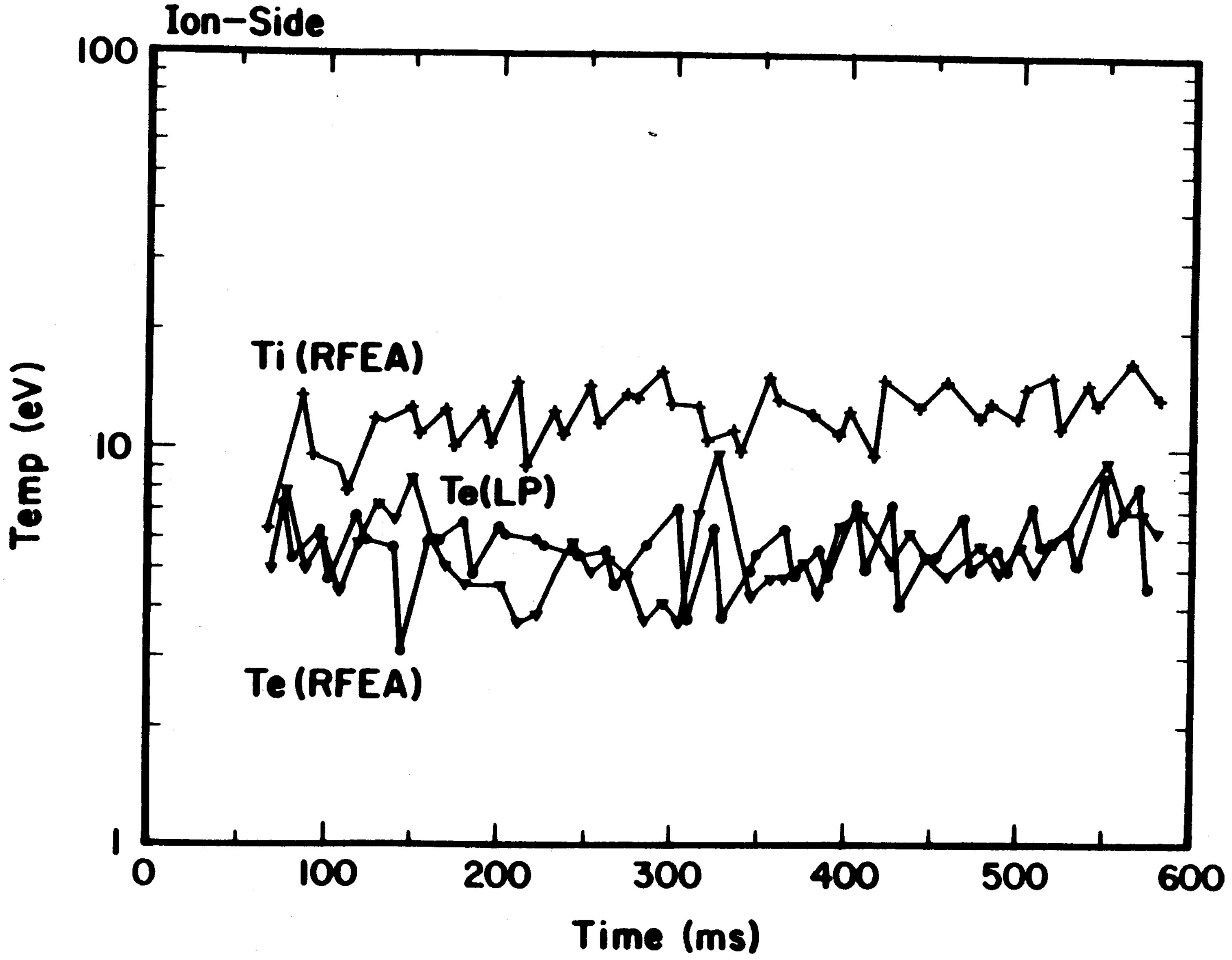

Figure 8(a)

m11/14/7

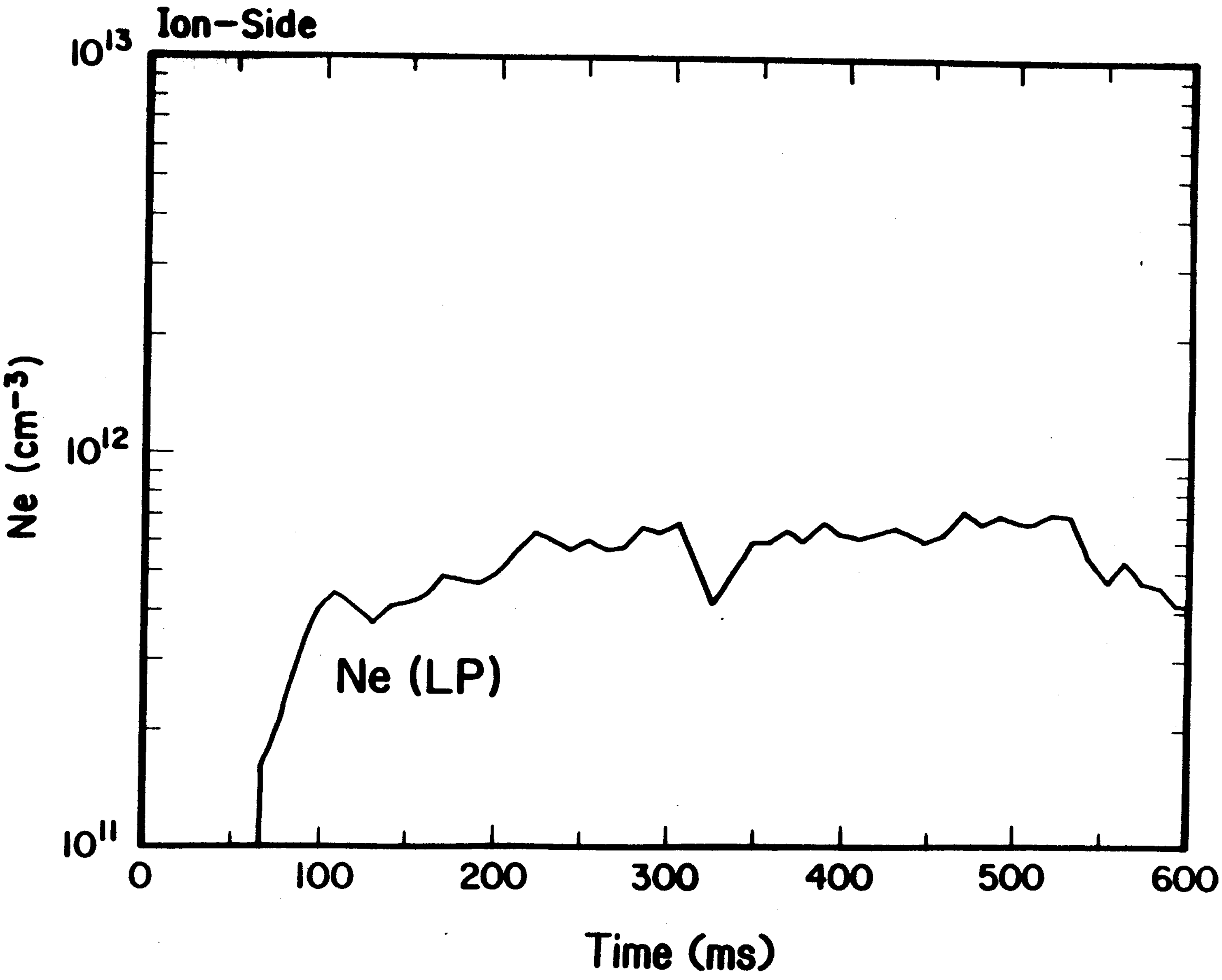
Ion-Side
10^{13}
10^{12}
10^{11}
Ne (cm^{-3})
Ne (LP)
0
100
200
300
400
500
600
Time (ms)

Figure 8(b)

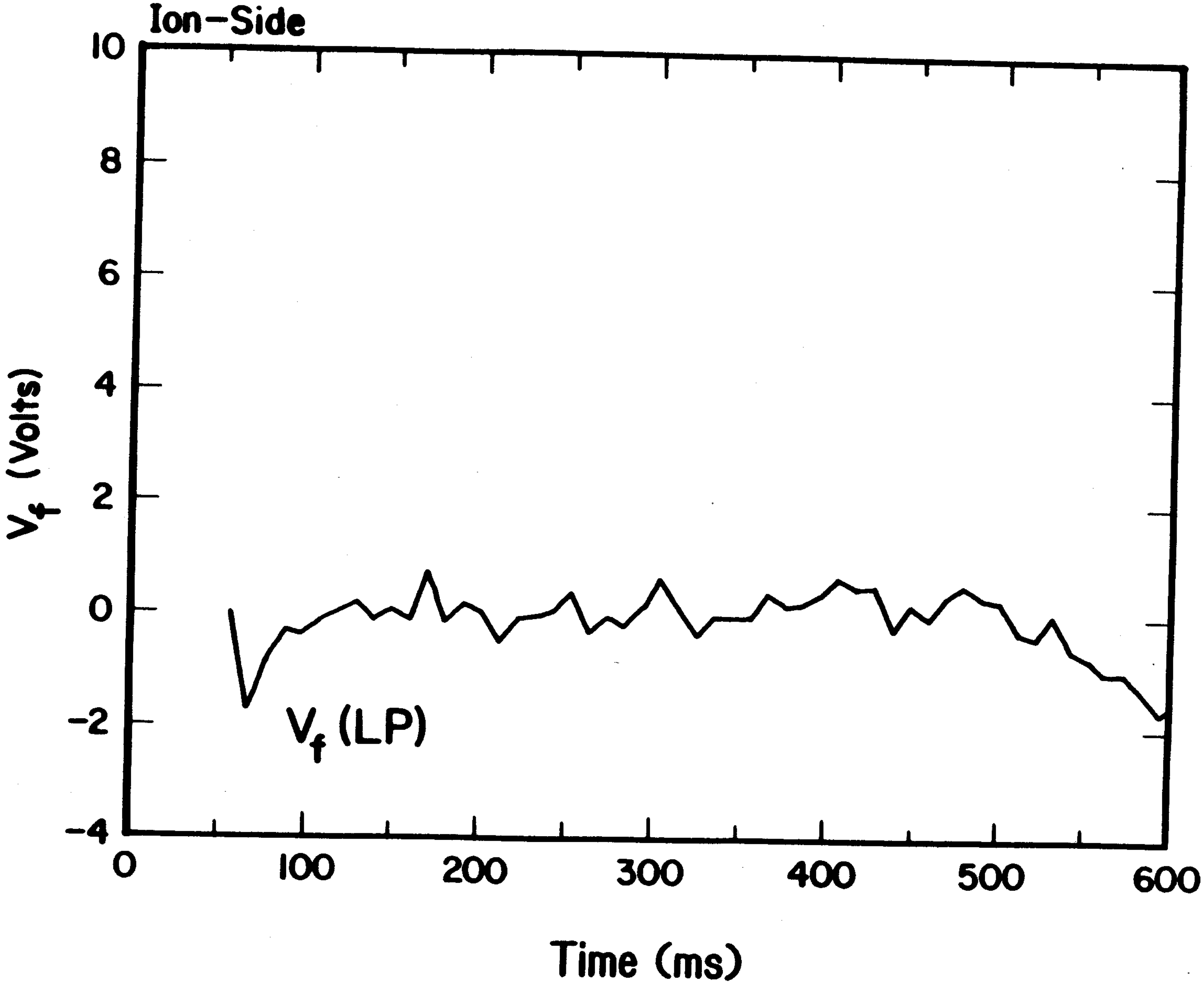

Figure 8(c)

8099/19/5